Title
Optimizing bone marrow lesion detection using dual energy CT.

Author
Huang, Hsu-Cheng

Publication Date
2017

Optimizing bone marrow lesion detection using dual energy CT

by

Hsu-Cheng Huang

THESIS

Submitted in partial satisfaction of the requirements for the degree of

MASTER OF SCIENCE

in

Biomedical Imaging

in the

[redacted]

ACKNOWLEDGEMENTS

I would like to thank my thesis advisor, Dr. Benjamin M. Yeh, M.D. for being an insightful mentor and helping me overcome all the obstacles. The door to Prof. Yeh's office was always open whenever I had a question. This project would not have reached its current stage without his inspiration, patience, and guidance. My sincere thanks also goes to Yuxin Sun for teaching me everything in the laboratory and devoting tremendous time helping me on the phantom project. Special thanks to Dr. Ramya Srinivasan, M.D., for sharing her brilliant thoughts and supporting all the experimental materials.

Thank you to my thesis committee members, Dr. Galateia Kazakia, PhD, Dr. Youngho Seo, Ph.D. and Dr. Henry VanBrocklin, Ph.D., for dedicating to education, generously giving their time and expertise to provide effective feedback on my research.

I would also like to thank Dr. Saloner, Dr. Martin, and MSBI faculty for all their efforts organizing the fantastic MSBI program.

I would like to thank my wife, Pei-Chen, for unfailing support throughout my year of study though she was pursuing her degree at the same time. Finally, I am forever grateful for my parents' continuous encouragement along the way.

Optimizing bone marrow lesion detection using dual energy CT.

Hsu-Cheng Huang

Introduction:

Bone metastasis is the third most common metastasis in cancer patients, causing intractable pain and debilitating complications. However, studies have shown that conventional single-energy computed tomography (SECT) has limitation in detecting subtle bone metastases without obvious osteolysis/osteosclerosis. We hypothesize that dual-energy computed tomography (DECT) can distinguish different composition in tumors and in healthy bone marrow, facilitating the detection of bone marrow metastases.

Methods:

We constructed 51 semi-anthropomorphic lumbar spine phantoms embedded with 75 simulated tumors (25 mild lytic, 25 isodense, and 25 mild sclerotic). These phantoms were initially scanned without outer torso phantom encasement, and then scanned again with outer torso phantom encasement under the same machine setting in a rapid-kilovoltage-switching DECT scanner. Two radiologists independently reviewed the virtual monochromatic reconstruction in 70 keV and material decomposition images (hydroxyapatite-water, water-hydroxyapatite, cortical bone-water, water-cortical bone). We recorded reviewer's response regarding the presence of tumors, tumor conspicuity score and image quality using 3-point Likert scales. The sensitivity and specificity of different reconstruction algorithms were evaluated with McNemar test. Wilcoxon signed rank test was used to evaluate the tumor conspicuity and image quality of different algorithms. Then we validate our testing algorithms by retrospectively reviewing patients' images in our institution.

Results:

Hydroxyapatite-Water material decomposition algorithm achieved higher sensitivity in detecting isodense lesions as compared to the 70 keV reconstruction (without torso phantom encasement: 94% vs 82%, $p=0.031$; with torso phantom encasement: 38% vs 18%, $p=0.013$). Hydroxyapatite-Water material decomposition algorithms also possessed higher tumor conspicuity score ($p<0.0001$) compared to 70 keV reconstruction, and was less affected by CT artifacts.

Conclusion:

DECT with hydroxyapatite-water material decomposition may help detect spine marrow metastases, especially for subtle isodense tumors. Further study in prospective clinical scans is warranted.

TABLE OF CONTENTS

Page

1. INTRODUCTION

2. MATERIALS AND METHODS

3. RESULTS

4. DISCUSSION

LIST OF TABLES

Page

LIST OF FIGURES

Page

1 INTRODUCTION

1.1 Background

Computed tomography(CT) has been increasingly utilized because of its capability of providing detailed information for disease diagnoses and treatment. In the United States(U.S.), 82 million CT scans were performed in 2016[1]. In particular, approximately 25% of all CT scans[2] were used for cancer staging or follow-up in compliance to many of the current oncologic guidelines. In cancer patients, bone is the third most common metastasis site with painful and untreatable consequences[3], and in U.S., more than 350,000 patients die each year with bone metastases, which might also contribute to their death[4]. Therefore, identification of bone metastasis is crucial for more accurate staging, re-staging, and tailoring treatment plan. However, studies have shown that the conventional single energy CT is limited in detecting subtle bone metastases without obvious osteolysis/osteosclerosis[5]. In a meta-analysis of diagnosing bone metastases, the sensitivity and specificity of CT were only 77 and 83 percent[6]. In most of these circumstances, other imaging modalities such as 99mTc-MDP (methylene diphosphonate) whole-body bone scintigraphy, positron emission tomography (PET)/CT, or magnetic resonance imaging(MRI) are required to increase diagnostic accuracy. However, each of these imaging modalities also has its own limitations. Bone scintigraphy is less sensitive for tumors with little or no osteoblastic activity, and can't differentiate bone metastases from other abnormalities with little tracer uptake, such as trauma or degenerative disease[7]. Though MRI and PET/CT have higher sensitivity and specificity on detecting bone metastases[8], the lack of availability, the long acquisition time, and the associated high cost hamper them from first-line usage.

The principle of dual-energy CT (DECT) technique is based on the unique k-edge characteristics and energy dependence of the photoelectric effect[9]. The likelihood of photoelectric absorption increases as the energy of an incident photon is more closely matched the K-shell binding energy. Substance with a high atomic number (Z) (e.g., iodine and calcium) absorb more low-energy photons (70-100 kVp) than high-energy photons; in contrast, human soft tissues primarily consisting with low atomic number elements (e.g., oxygen and hydrogen) show no substantial difference in absorption between high and low energy photons because neither the high nor low energy x-ray beams match their binding energy. Therefore, the attenuation differences between the high and low energy beams facilitate DECT to differentiate and classify different tissues based on their distinct levels of photon absorption[10]. Several studies have shown that DECT can detect occult bone fractures and bruises when such injuries are not apparent on radiographs and conventional CT[11,12]. DECT has also been used to reduce metallic artifacts through high keV monochromatic reconstructions that reduce photon starvation and beam hardening[13]. These applications of DECT on skeletal system gave us incentive to further explore the utilization of DECT on detecting bone metastases. To our knowledge, there is only one study discussing the potential of DECT in visualizing bone metastasis[14]. That study focused on calcium-iodine material decomposition and concluded that contrast-enhanced DECT could improve detection of small bone metastases.

1.2 Project Goals:

Bone metastases can be either osteolytic or sclerotic, depending on whether osteoclast or osteoblast predominates. However, in most tumors, bone resorption and formation usually co-exist, leading to a dynamic equilibrium. In between the two ends of the tumor spectrum, nearly-isodense metastases fall into the category that is usually missed because of the difficulty in discerning subtle density difference between tumor and background bone marrow. Therefore, the aim of this project is to optimize CT bone metastases detection by dual energy CT, with special focus on nearly isodense lesions. In terms of the algorithm, rather than choosing the calcium-iodine material decomposition, we would like to focus on the bone-water material decomposition to reflect the pathological nature of tumors. We assume that the bone-water material decomposition can make bone metastases more discernable because the tumors are primarily composed of these two basis materials.

Since lumbar spine is the most common anatomical site for bone metastases[15], we plan to build several lumbar spine phantoms embedded with different simulated metastatic tumors. Each phantom will be scanned by DECT and reconstructed in different basis-pair. Then we will perform a quantitative analysis of acquired images to determine the optimal scan parameters and develop material decomposition post-processing algorithms which can differentiate water (major composition of bone tumor) from calcium (major composition of normal bone). Finally, we will validate our algorithm with retrospective patient CT scans which were initially read as negative for bone marrow lesions, but later detected by other imaging modalities or at follow up CT.

2 MATERIALS AND METHODS

2.1 Phantom:

2.1.1 Phantom material:

2.1.1.1 Simulated bone marrow compartment composition

The vertebral bone marrow compartment is composed of marrow adipose tissue, bone mineral, hematopoietic and stromal cells (ground substance). To simulate the vertebral marrow compartment, we tested different materials with various matrices composed of known ratios of commercially available wax or oil (simulating fat), calcium containing powder (simulating bony mineral), and polyurethane rubber (VytaFlex-30, Smooth-On, PA, USA) (simulating ground substance). The fat fraction in the simulated vertebral marrow compartment was targeted to be 45% based on the fact that bone marrow fat fraction increases with age (in lumbar spine), and is 45% on average in the 51-60 age group[16]. For determining the Hounsfield unit (HU) in simulated vertebral marrow compartment, we measured the vertebral marrow compartment hounsfield unit at L3 vertebra from 20 patients' abdomen CT scans (patients age between 51-60, excluding those who had pathology in lumbar spine), getting the average HU of L3 marrow compartment being 170. Thus we made our phantom vertebral marrow compartment with a target HU of 170.

2.1.1.2 Simulated metastatic tumors composition

Metastatic bone tumors are caused by cancer cells invading the bone marrow stroma and developing angiogenesis. Metastatic marrow tumors do not contain fat unless the tumor cells are originated from primary fat-containing tumors. Therefore, the simulated metastasis tumors were composed of solely calcium containing powder (simulating bone mineral) and polyurethane rubber (simulating water in soft tissue component from tumors). We made simulated tumors with three different densities: 130 HU (mild lytic), 170 HU (isodense), and 210 HU (mild sclerotic) at 70 keV to simulate the spectrum from osteolytic to osteoblastic bone metastases.

2.1.1.3 Fat equivalent material:

We initially tested materials which were solids at room temperature, including ground machinable wax, ground paraffin powder, candle wax powder (Vybar103, The Candlewic Company, USA). However, it was difficult to avoid air bubbles when mixing these powder with Vytaflex. Moreover, the air bubbles would not disappear in the vacuum chamber, thereby leading to false-positive results of the material decomposition algorithm by artificially increasing the dual energy ratio. We also tried to melt the powder and mixed them with Vytaflex before they cooled down. However, when poured into Vytaflex, all types of melted wax turned back to solid state and became chunky, resulting in inhomogeneous phantoms. Therefore, for the fat component, we tested the canola oil, which was liquid at room temperature. Canola oil mixed evenly with Vytaflex initially, but slowly seeped out soon before the mixture completely cured. This unfortunate phenomenon made our fat fraction inaccurate and inconsistent.

In the end, we chose commercially available coconut oil because its melting point was 75°F. Such a specific physical property enables coconut oil to mix perfectly with Vytaflex in its liquid state, and then solidify quickly once being cooled, without seeping out throughout the curing process.

2.1.1.4 Ground substance and water equivalent material

We initially considered using pure Vytaflex as the ground substance and water equivalent material because its CT number is known to be 0 HU at 70 keV. We tested our hypothesis by making a test phantom constructed with a simulated background bone marrow compartment in the center (average 178 HU on 70keV, Figure 1 left), surrounded by a serial of simulated bone lesions ranging from 110 HU to 200 HU on 70keV to serve as the mild osteolytic, isodense, and mild sclerotic lesions. In Figure 1, under 70 keV, the lesion at 4 o’clock had almost the same CT number (182 HU) as the background bone marrow compartment, which represented an isodense bone metastatic lesion. Also, the histogram (Figure 1 middle) of the background bone marrow compartment and the lesion were almost entirely overlapped. Unexpectedly, the GSI scatter plots (Figure 1 right) with water-cortical bone basis pair derived from DECT showed that the background bone marrow compartment (pink dots) and the lesion (green dots) largely overlapped with each other, which meant we could not differentiate them either.

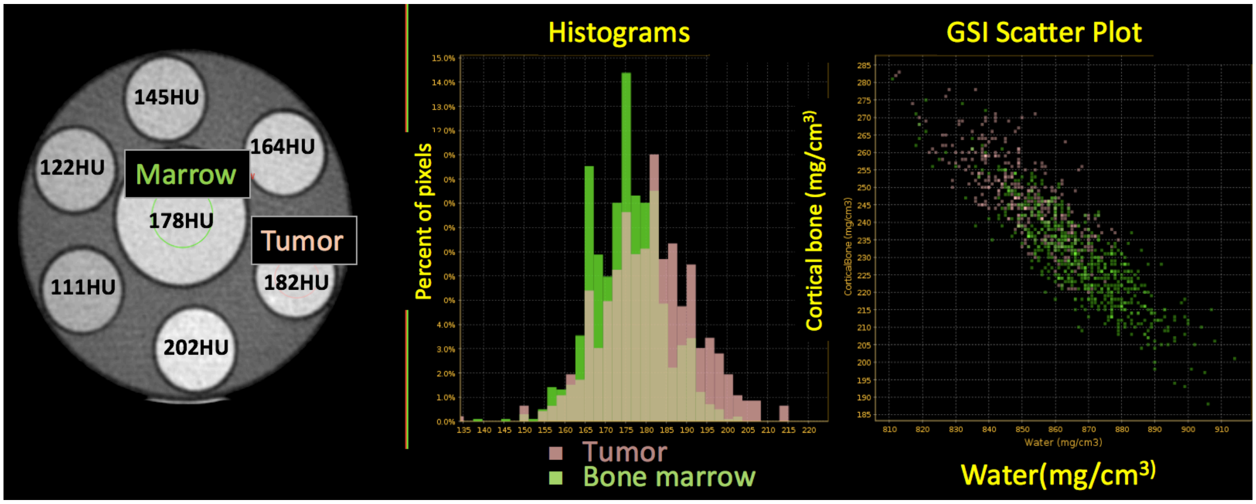

Figure 1. The simulated marrow compartment (center circle) and the simulated tumor with the similar CT number (4 o'clock circle). Their histogram on 70 keV reconstruction and material decomposition GSI scatter plot were largely overlapped.

After analyzing the spectral curve of the pure Vytaflex (Figure 2), we found that the curve of pure Vytaflex showed negative CT number in the low-energy image and plateau after 120keV. This characteristic HU spectral curve actually more similar to the curve of fat (the yellow line) rather than that of water (the green line). This finding explained why the material decomposition algorithm of DECT could not differentiate the simulated lesions from the simulated background bone marrow compartment, for none of them contained water equivalent material. To adjust the spectral curve towards water equivalent, we considered mixing polyurethane rubber with another element that has a slightly higher atomic number to carbon (i.e., the principal element of fat) in order to increase its attenuation in the low-energy images[17]. Therefore, we checked the periodic table and selected Sodium and Magnesium as our candidate elements. We tested NaCl doped Vytaflex and magnesium doped Vytaflex with different concentrations. The settling phenomenon was more obvious in NaCl-Vytaflex mixture because NaCl has a higher density than magnesium. After serial testing, we found that doping 7% magnesium powder with 93% Vytaflex generated a flatter spectral curve from 40keV to 140keV, which was more favorable to serve as a water equivalent phantom material in clinical relevant x-ray energy (Figure 3).

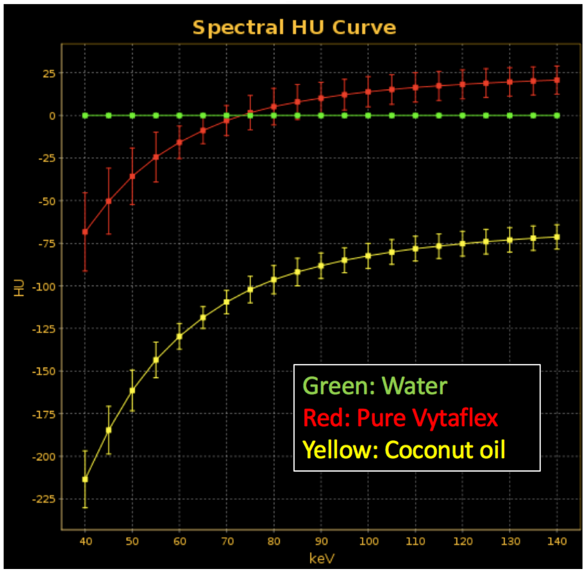

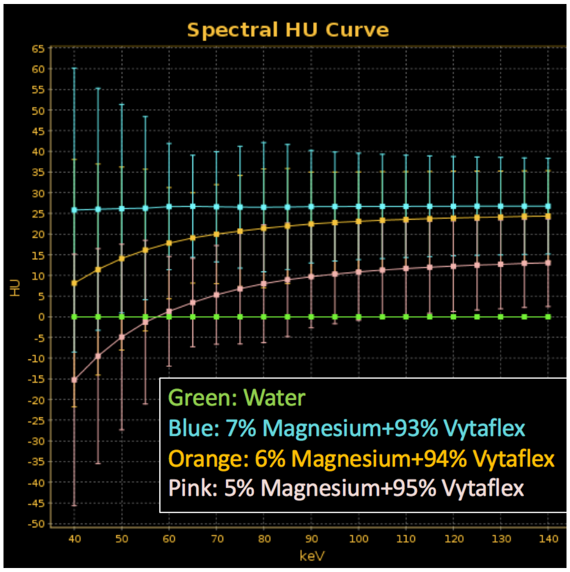

Figure 2. The spectral curve of pure Vytaflex is much similar to coconut oil rather than water.

Figure 3. The spectral curve of Vytaflex mixed with 7% magnesium resulted in a flat curve from 40keV to 140keV, similar to water.

We performed another test on comparing the discrimination power between 70 keV reconstruction and material decomposition algorithms with a new phantom made from magnesium doped Vytaflex (Figure 4). Using 70 keV reconstruction, the background bone in the center circle and the tumor phantom at 4 o'clock had the same CT number (152 HU, Figure 4 left), which failed to differentiate the tumor from normal bone marrow compartment. However, the tumor at 4 o'clock was clearly discernable in the water-cortical bone material decomposition image using DECT (Figure 4 middle). The GSI scatter plot (Figure 4 right) also demonstrated the separation of the simulated background bone marrow compartment and the simulated tumors.

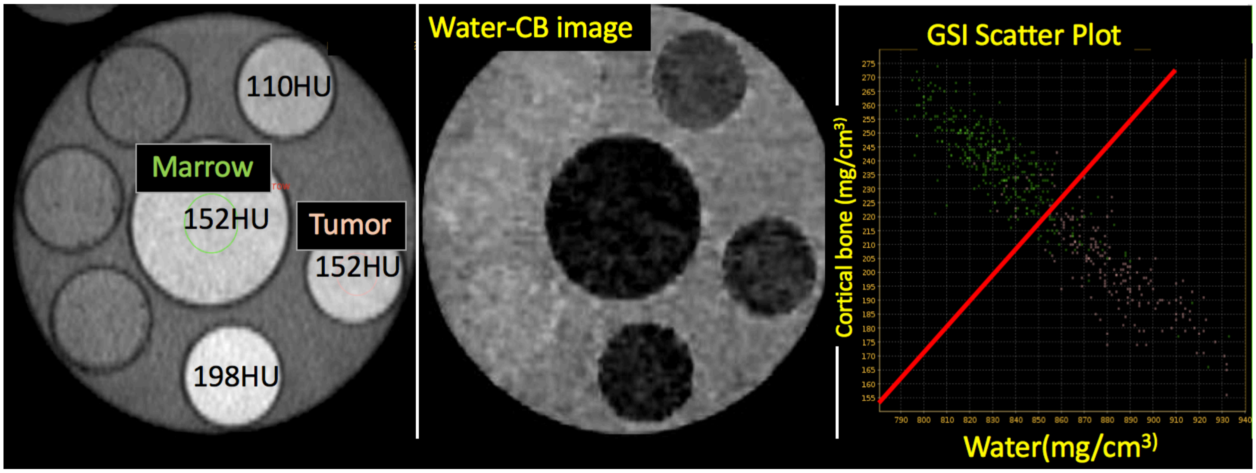

Figure 4. New phantom made from magnesium doped Vytaflex. The simulated marrow compartment (center circle) and the simulated tumor with the similar CT number (4 o'clock circle) on 70 keV reconstruction and cannot be differentiated. In material decomposition Water-CB image (middle), the tumor (4'oclock) was discernable from the marrow (center). The GSI scatter plot (right) also showed that the tumor and the marrow were clearly separated.

2.1.1.5 Bone equivalent material

We used commercial available bone meal powder (KAL, Nutraceutical Corporation, Utah) to serve as the bone equivalent material not only because it contains the major salts in human bone, such as calcium, phosphorus, and magnesium[18], but also because the bone powder could mix evenly in Vytaflex.

2.1.2 Phantom construction

2.1.2.1 Spine mold (Figure 5A)

We 3D printed a 300mm cylindrical column in the shape of a human lumbar spine. The distance between anterior vertebral body to spinous process is 72mm, and the distance between bilateral transverse processes is 74mm, which is the average size of adult L3 vertebra. We built 9 identical hollow molds (each has 3 cm in height) out of the 3D printed spinal column with silicon (MoldMax-30, Smooth-On, PA, USA). These hollow molds were prepared for future casting with simulated bone marrow compartment mixture.

2.1.2.2 Simulated tumors (Figure 5B)

We manually mixed the bone meal 10.5%, 13.5% and 16.5% by weight with the magnesium doped Vytaflex to made 3 mixtures in 130HU, 170HU, 210 HU. Placed the mixture on the vortex mixer for 2 minutes and poured the mixture immediately into ice cube trays (spherical shape with 1.8cm in diameter) and let them cure overnight.

2.1.2.3 Spine phantoms (Figure 5C)

We manually mixed bone meal 16.5% and liquid coconut oil 45% by weight with the magnesium doped Vytaflex to produce bone marrow compartment material in the desired CT number of 170 HU at 70 keV. We placed the mixture on the vortex mixer for 2 minutes and poured them into the spine molds. Then we embedded aforementioned simulated tumors into the uncured bone marrow compartment material and placed the spine molds into refrigerator overnight. The cooling process could accelerate the solidification of coconut oil, thus preventing the oil from seeping out and mitigating the settling effect of the bone meal and magnesium powder. For each segment of spine phantom, we divided it into two compartments, left and right. For each compartment, we either left it blank (no lesion) or embedded one lesion. In the end, 51 segments of spine were randomly embedded with 0 to 2 different kinds of tumors.

2.1.2.4 Inner encasement phantom (Figure 5D)

We made a hollow housing tube (12cm in diameter and 30cm in length) by casting the 3D printed spine column in a polyethylene tube with pure Vytaflex. This inner encasement tube could accommodate 7 segments of spine phantoms and allowed us to scan multi-segments at the same time.

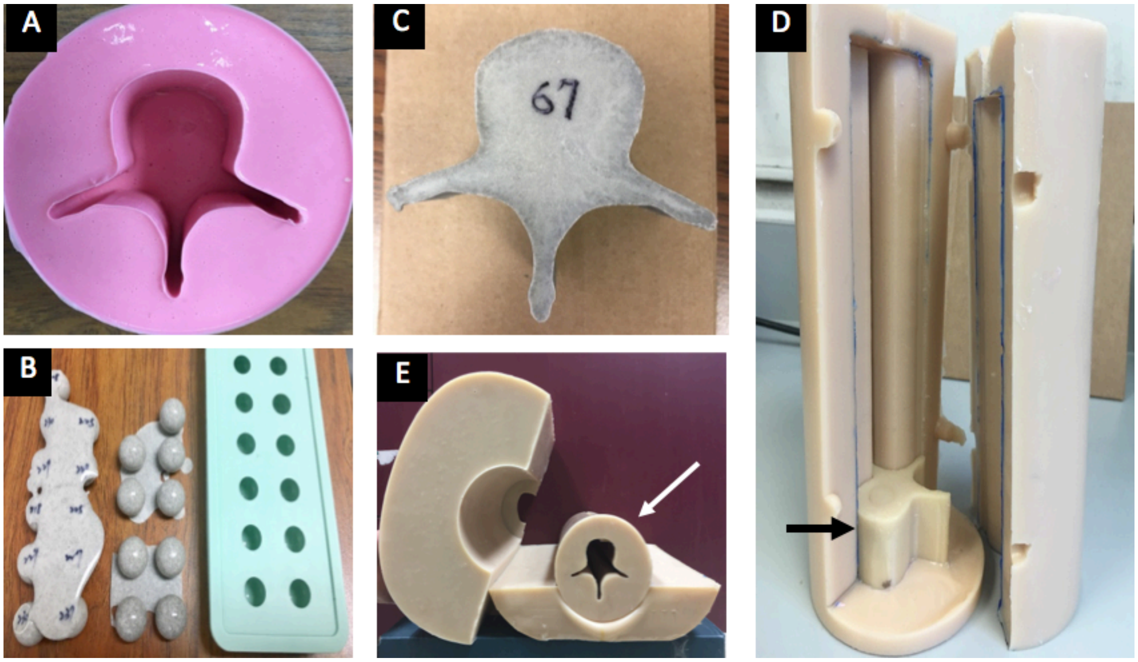

Figure 5. A) Silicon mold of 3-D printed spine. B) Identical tumors made from ice cube trays. C) Spine phantom with tumor embedded. D) Inner encasement, partly opened, with one spine (arrow) phantom in place. Room for 6 other spine phantoms is present. E) Torso encasement, partly opened, with inner encasement (arrow) in place.

2.1.2.5 Adult human torso size phantom (Figure 6)

We casted the inner encasement in a CIRS CT phantom (model 007TE-06 small adult, 30cm in anterior-posterior distance, 20cm in left-right distance) with Vytaflex. We put the spine phantoms into the inner and torso encasement to simulate human scans (Figure 6 right).

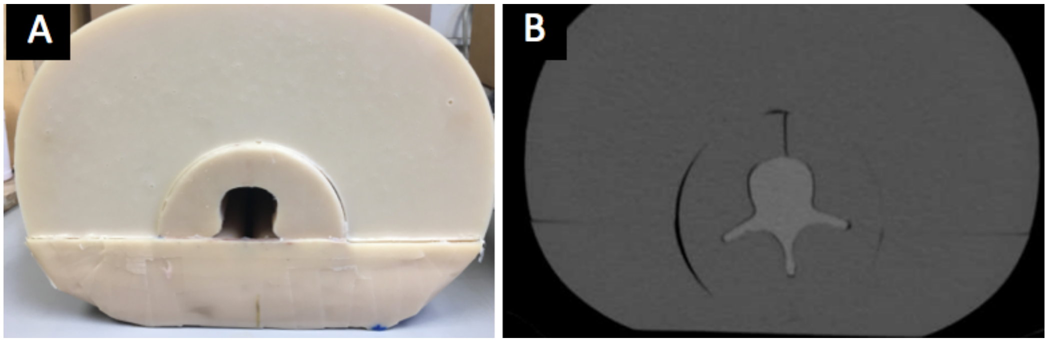

Figure 6. A) Full assembled phantom B) CT image of the full assembled phantom

2.2 Patient selection:

We retrospectively searched the PACS system in the UCSF medical center from January 2014 to March 2017 with the keywords “spine metastases”, “vertebral metastases”, and ”vertebrae metastases”. The inclusion criteria was (a) >18 years of age; (b) confirmed spine metastases by bone scintigraphy, MRI or PET scan, and underwent DECT scans of abdomen within 30 days either before or after the diagnosing image. (c) the confirmed lumbar spine metastases were not obvious on the 70 keV reconstruction in DECT (defined as the difference of CT number between tumor and normal background bone marrow compartment less than 100HU). The exclusion criteria was (a) underwent spine surgery or vertebralplasty which introduced significant image artifacts; (b) all metastatic lesions smaller than one centimeter.

2.3 Image protocol and post processing:

First, we scanned one of the torso phantom encasement with a rapid-voltage-switching DECT scanner (Discovery CT750 HD scanner, GE Healthcare, Milwaukee, WI) in standard single-energy CT mode with tube current modulation in order to calculate the optimal radiation dose. We setup the protocol on DECT mode with the same $CTDI_{vol}$ as that in standard single-energy CT mode. Then the 51 spine-only phantoms and the 51 spine phantoms with human torso encasement were scanned with the identical setting on in dual-energy spectral CT mode. The scanning parameters were as follows: dual-energy helical scanning with 80/140-kVp fast switching, GSI protocol number 31, tube current fixed at 360 mA; rotation time, 0.5 second; helical pitch, 0.984:1. The $CTDI_{vol}$ was 12.92 mGy. The CT images were reconstructed with the following parameters: DFOV (displayed field of view), 25.1cm x20cm; reconstructed voltage, 70 keV; slice thickness, 1.25 mm.

The patient and phantom studies were reconstructed in axial slices using a standard DECT workstation (GSI Viewer, Advantage Windows server 2.02, GE Healthcare) with the following five sets of postprocessed images: 70 keV virtual monochromatic spectral images (resembling conventional 120 kVp polychromatic CT images)[19]; material decomposition in hydroxyapatite-water(HAP-Water), water-hydroxyapatite(Water-HAP), cortical bone-water(CB-Water), and water-cortical bone(Water-CB). The hydroxyapatite-water basis pair was the stock algorithm built in the server. The cortical bone-water was a new basis-pair we created by importing the mass attenuation coefficients of cortical bone from the National Institute of Standards and Technology (NIST) database[20] into the server (Figure 7). The 70 keV images were set in the default clinical vertebra window (W:2000, L:350). The default window level of HAP-Water and Water-HAP were 500/150 mg/cm^3 and 300/1000 mg/cm^3. The default window of cortical bone-water, and water-cortical bone were 1000/300 mg/cm^3 and 300/1000 mg/cm^3.

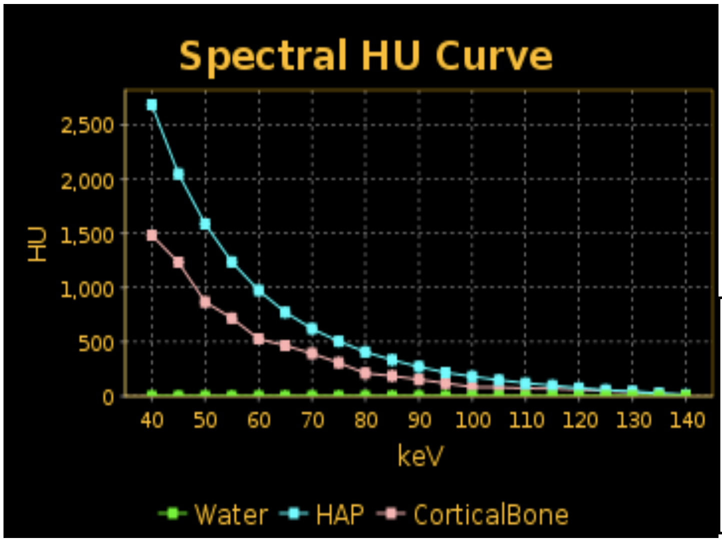

Figure 7. Spectral HU curve of water, cortical bone, and hydroxyapatite from NIST database.
Green: Water
Pink: Cortical bone
Blue: Hydroxyapatite

2.4 Quantitative and qualitative image analysis

The reviewers were blinded to both the presentation and types of tumors in the phantoms they reviewed. The five sets of images were accessed by two board-certified radiologists (B.Y. and R.S., with 20 and 6 years of experience, respectively) on the Advantage for Windows thin client server 2.02 (GE Healthcare) independently for the presence or absence of tumors. The FOV was fixed at 36.3 x 20 cm for all images on a MacBook Pro (Apple Inc.) monitor with 226 dpi. First, reviewers read the 70 keV virtual monochromatic images in default window-level setting to diagnose if tumors presented or not, and to judge the image quality of reconstruction according to a 3–point Likert score: 0, artifact makes image non-diagnostic; 1, artifact present but still be able to make a diagnosis; 2, no significant artifact. If there were no tumors seen on the default window, then reviewers could adjust the window-level setting as needed and re-evaluate the images. Whenever a tumor was identified, the readers further determined the tumor conspicuity according to a 3–point Likert score: 1, only seen with non-standard windows; 2, faintly seen with default window; 3, clear cut abnormality on default window. After finishing the 70keV images, readers read the rest of 4 material decomposition images in sequence, following the aforementioned protocol.

2.5 Statistical analysis

Continuous variables were expressed as means ± standard deviations. The Cohen's kappa test was performed to evaluate the inter-observer agreements regarding the presence of tumor. The agreements were categorized into 5 groups[21]: <0.20: Slight agreement; 0.20–0.40: Fair agreement; 0.41–0.60: Moderate agreement; 0.61–0.80: Substantial agreement; 0.81–1.00: Almost perfect agreement.

The sensitivity, specificity of the five sets of images on phantoms were calculated on per lesion basis. McNemar test was used to compare the tumor detection rates of the 5 algorithms. Comparison of tumor conspicuity and image quality between 70keV and 4 different material decomposition images was conducted with the Wilcoxon signed rank test. All statistical analyses were performed with commercially available software (StataCorp. 2003. Stata Statistical Software: Release 8. College Station, TX: StataCorp LP.). Those p values smaller than 0.05 were considered statistically significant.

3 RESULT

3.1 Phantom results

We scanned 51 spine phantoms without torso encasement first and then scanned these spine phantoms again with human torso size phantom encasement. Totally 102 segments of spine phantoms were scanned, giving 204 compartments in which 50 of them contained lytic tumors, 50 contained isodense tumors, and 50 contained sclerotic tumors. 54 compartments were left blank without embedding tumors. The HU of all tumors and surrounding bone marrow compartment were confirmed by CT ROI measurements. The mean difference and standard deviation between tumors and surrounding bone marrow compartment were 43.1 ± 12.7HU in lytic tumors, 9.4 ± 5.4HU in isodense tumors, and 39.6 ± 9.6HU in sclerotic tumors.

3.1.1 Kappa analysis

Interobserver agreement for all phantoms (with- and without torso encasement) was almost perfect (Kappa=0.82; 95% CI,0.76-0.88). Subgroup analysis found excellent agreement in spine phantoms (Kappa=0.94; 95% CI, 0.86-1), and substantial agreement in torso encasement phantoms (Kappa=0.68; 95% CI, 0.6-0.77). Further subgroup analysis in the torso encasement phantom images showed that the agreement of diagnosis is better in 70 keV, HAP-Water, and

CB-Water reconstructions (Kappa=0.84, 0.76 and 0.73), but only fair to moderate agreement in Water-HAP and Water-CB reconstructions (Kappa = 0.32 and 0.51).

3.1.2 Sensitivity and specificity (without and with torso phantom encasement)

We combined the reading results from both readers and summarized the sensitivity and specificity by different reconstruction algorithm in Tables 1. The 70 keV reconstruction resembled the conventional 120 kVp polychromatic CT images under standard body habitus, and was considered as the reference standard to be compared with.

In spine phantoms without torso encasement, the sensitivity in HAP-Water and Water-CB algorithms were significantly better than the 70 keV reconstruction ($p=0.031$ and 0.003). The sensitivity in Water-HAP algorithm was worse than the 70 keV reconstruction ($p=0.016$). The difference of sensitivity between Water-CB algorithm and 70 keV reconstruction were unremarkable ($p>0.05$). In torso encasement phantoms, the sensitivity in HAP-Water algorithm was significantly better than the 70 keV reconstruction ($p=0.021$). The comparison of sensitivity between CB-Water and 70 keV reconstruction were unremarkable ($p>0.05$), while those of the Water-HAP and Water-CB reconstruction were inferior than the 70 keV reconstruction($p<0.001$). The comparison of specificity between each algorithm and 70 keV reconstruction using

McNemar test all showed no statistically significant difference. The data are summarized in Table 1a and Table 1b.

Table 1a: Spine phantom without encasement

CT image reconstruction	Sensitivity(%)	p value (sensitivity)	Specificity(%)
70 keV	94% (141/150) [90.7%; 97.3%]		96.3% (52/54) [93.7%; 98.9%]
HAP-Water	98% (147/150) [96.1%; 99.9%]	0.031*	98.2% (53/54) [96.3%;100%)
Water-HAP	85.3% (128/150) [80.5%; 90.2%]	$0.016^{\#}$	100% (54/54) [100%; 100%)
CB-Water	100% (150/150) [100%; 100%]	0.003*	98.2% (53/54) [96.3%;100%)
Water-CB	96% (144/150) [93.3%; 98.7%]	0.439	100% (54/54) [100%; 100%]

Table 1b: Spine phantom with torso encasement

CT image reconstruction	Sensitivity(%)	p value (sensitivity)	Specificity(%)
70 keV	72% (108/150) [65.8%; 78.2%]		92.6% (50/54) [89%; 96.2%]
HAP-Water	78.7% (118/150) [73.1%; 84.3%]	0.021*	92.6% (50/54) [89%; 96.2%]
Water-HAP	28.7% (43/150) [22.5%; 34.9%]	$<0.001^{\#}$	96.3% (52/54) [93.7%;98.9%]
CB-Water	66% (99/150) [59.5%; 72.5%]	0.16	98.2% (53/54) [96.3%;100%]
Water-CB	38.7% (58/150) [32%; 45.4%]	$<0.001^{\#}$	98.2% (53/54) [96.3%;100%]

Table 1a: Spine phantom without encasement. Table 1b: Spine phantom with torso encasement. Sensitivity and specificity with the respective 95% confidence intervals based on 150 lesions in 204 compartments of spine. (* The sensitivity which is significantly better than 70 keV; # The sensitivity which is significantly worse than 70 keV on McNemar test).

Note: Data in parentheses are numbers used to calculate percentage, and data in brackets are 95% confidence interval. The p values are testing against the 70 keV reconstruction.

3.1.3 Sensitivity and specificity (by phantom type and lesion type)

In spine phantoms with isodense tumors, the sensitivity of HAP-Water and CB-Water algorithms were significantly better than that of the 70 keV reconstruction (for HAP-Water: 94% v.s. 82%, p=0.031; for CB-Water: 100% v.s. 82%, p= 0.004). For osteolytic and sclerotic lesions in spine phantoms, differences among the 5 algorithms were unremarkable.

In torso encasement phantoms with isodense tumors, the tumor detection rate of HAP-Water was also significantly better than 70 keV reconstruction (38% v.s. 18%, p=0.013) (Figure 8). For osteolytic and sclerotic lesions, the sensitivity of Water-HAP and Water CB algorithms were worse than the 70 keV reconstruction (p<0.0001).

Table 2 shows the subgroup analysis by lesion type (lytic, isodense, sclerotic) and by phantom type (without and with torso encasement).

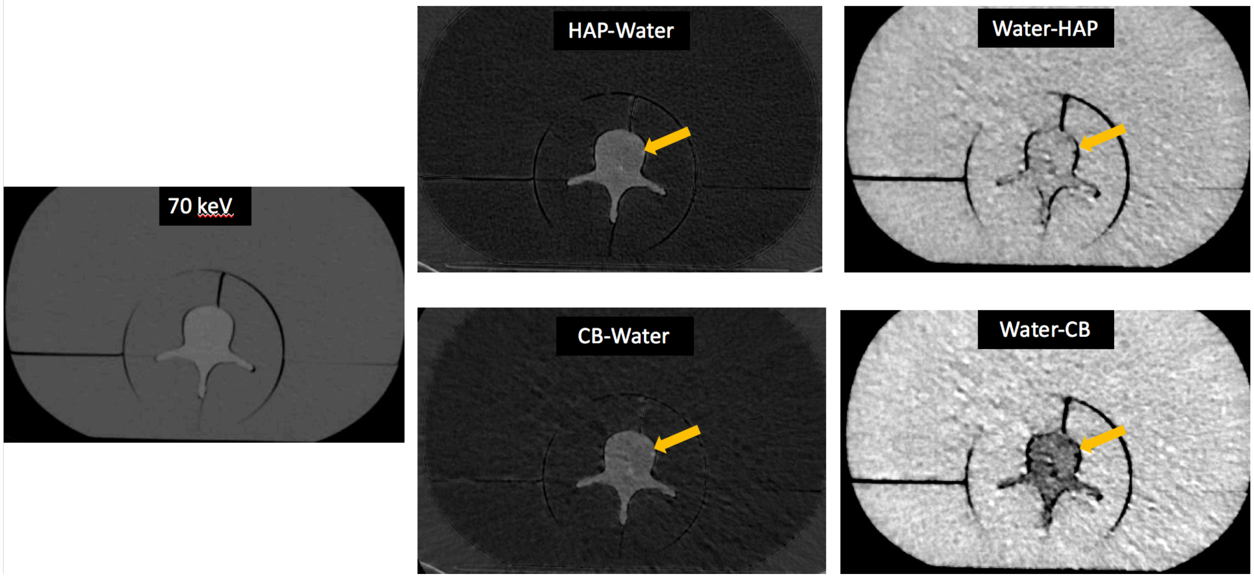

Figure 8. A spine phantom with torso encasement and an isodense tumor embedded in the left side of vertebral body. The tumor could not be detected in 70 keV image because the identical density from bone marrow. In HAP-Water and CB-Water reconstructions (middle row), the tumor was slightly hypodense because it contained less calcium. There was reciprocal change in Water-HAP and Water-CB reconstructions (right row): the tumor was slightly brighter than background marrow because of more water equivalent material in the tumor.

Table 2a: Spine phantom without encasement

CT reconstruction images	Sensitivity % (95% CI)			p value (comparing sensitivity)			Specificity % (95% CI)		
	Lytic	Isodense	Sclerotic	Lytic	Isodense	Sclerotic	Lytic	Isodense	Sclerotic
70 keV	100 (100)	82 (74.6; 89.4)	100 (100)				96.3 (92.7; 99.9)	96.3 (92.7; 99.9)	96.3 (92.7; 99.9)
HAP-Water	100 (100)	94 (89.4; 98.6)	100 (100)	1	0.031*	1	98.2 (95.6; 100)	98.2 (95.6; 100)	98.2% (95.6; 100)
Water-HAP	98 (95.3; 100)	66 (56.9; 75.1)	92 (86.8; 97.2)	1	0.15	0.12	100 (100)	100 (100)	100 (100)
CB-Water	100 (100)	100 (100)	100 (100)	1	0.004*	1	98.2 (95.6; 100)	98.2 (95.6; 100)	98.2 (95.6; 100)
Water-CB	100 (100)	88 (81.8; 94.3)	100 (100)	1	0.6	1	100 (100)	100 (100)	100 (100)

Table 2b: Spine phantom with torso encasement

CT reconstruction images	Sensitivity % (95% CI)			p value (comparing sensitivity)			Specificity % (95% CI)		
	Lytic	Isodense	Sclerotic	Lytic	Isodense	Sclerotic	Lytic	Isodense	Sclerotic
70 keV	98 (95.3; 100)	18 (10.6; 25.4)	100 (100)				92.6 (87.6; 97.6)	92.6 (87.6; 97.6)	92.6 (87.6; 97.6)
HAP-Water	98 (95.3; 100)	38 (28.7; 47.3)	100 (100)	1	0.013*	1	92.6 (87.6; 97.6)	92.6 (87.6; 97.6)	92.6 (87.6; 97.6)
Water-HAP	28 (19.4; 36.6)	26 (17.6; 34.4)	32 (23; 41)	$<0.0001^{\#}$	0.48	$<0.0001^{\#}$	96.3 (92.7; 99.9)	96.3 (92.7; 99.9	96.3 (92.7; 99.9
CB-Water	92 (86.8; 97.2)	34 (24.9; 43.1)	72 (63.4; 80.6)	0.37	0.09	$0.0001^{\#}$	98.2 (95.6; 100)	98.2 (95.6; 100)	98.2 (95.6; 100)
Water-CB	44 (34.5; 53.5)	24 (15.8; 32.2)	48 (38.4; 57.6)	$<0.0001^{\#}$	0.49	$<0.0001^{\#}$	98.2 (95.6; 100)	98.2 (95.6; 100)	98.2 (95.6; 100)

Table 2a: Spine phantom without encasement
Table 2b: Spine phantom with torso encasement.
Sensitivity and specificity with the respective 95% confidence intervals based on lesion types. (* The sensitivity which is significantly better than 70 keV; # The sensitivity which is significantly worse than 70 keV on McNemar test).
Note: There were 50 lytic tumors, 50 isodense tumors, and 50 sclerotic tumors. There were 54 compartments without tumor embedded. The p values are testing against the 70 keV reconstruction.

3.1.4 Sensitivity and Specificity (Combined basis pair)

We combined the diagnostic results from HAP-Water, Water-HAP images because they were basis pairs and the images were generated simultaneously. If the tumor was identified in either the HAP-Water or Water-HAP algorithm, we recorded the results of reading as positive. The sensitivity of both the “combined HAP-Water” and “combined CB-Water” algorithms were not significantly different from the HAP-Water algorithm or the CB-Water algorithm alone, regardless of lesion type or phantoms type ($p>0.05$).

3.1.5 Tumor conspicuity (Figure 9)

In spine phantoms without torso encasement, the tumor conspicuity scores were significantly (all $p < 0.0001$) better in the HAP-Water, CB-Water and Water-CB algorithms (median score, 3; range, 1–3) compared to the 70-keV images (median score, 2; range, 1–3) and Water-HAP images (median score, 2; range, 1–3). With torso phantom encasement, the tumor conspicuity scores were significantly better in the HAP-Water algorithm ($p<0.0001$) compared to the 70-keV images. Tumor conspicuity in Water-HAP and CB-Water images were lower than the 70-keV images ($p=0.017$ and 0.038 respectively).

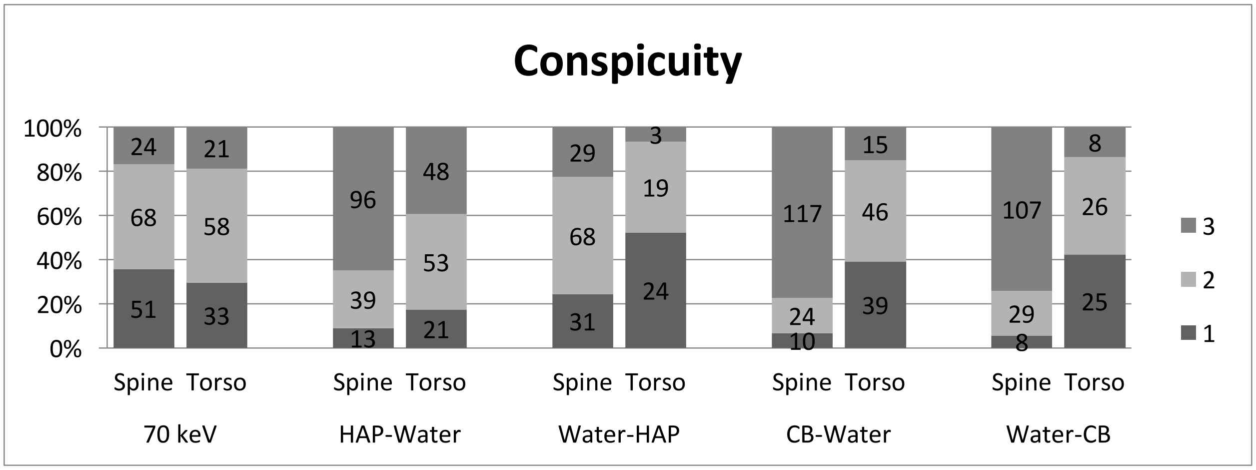

Figure 9: Tumor conspicuity score in 5 different algorithms, sorted by phantom type. Score 1, only seen with non-standard windows; Score 2, faintly seen with default window; Score 3, clear cut abnormality on default window. (“Spine” stood for spine phantom without torso phantom encasement; “Torso” stood for spine phantom with torso phantom encasement.)

3.1.6 Image Quality (Figure 10)

All 4 material decomposition images got lower scores on image quality compared to 70-keV reconstructions (p<0.0001), both in spine-only phantoms or in spine phantoms with torso encasement. Comparing the quality scores between spine phantom without and with torso encasement in each algorithm, the quality scores were significantly lower when scanned with torso encasement in Water-HAP, CB-Water, and Water-CB images (p=0.0001). In contrast, the quality scores did not differ between without and with torso phantom encasement in 70 keV and HAP-Water images (p=0.1 and 0.13).

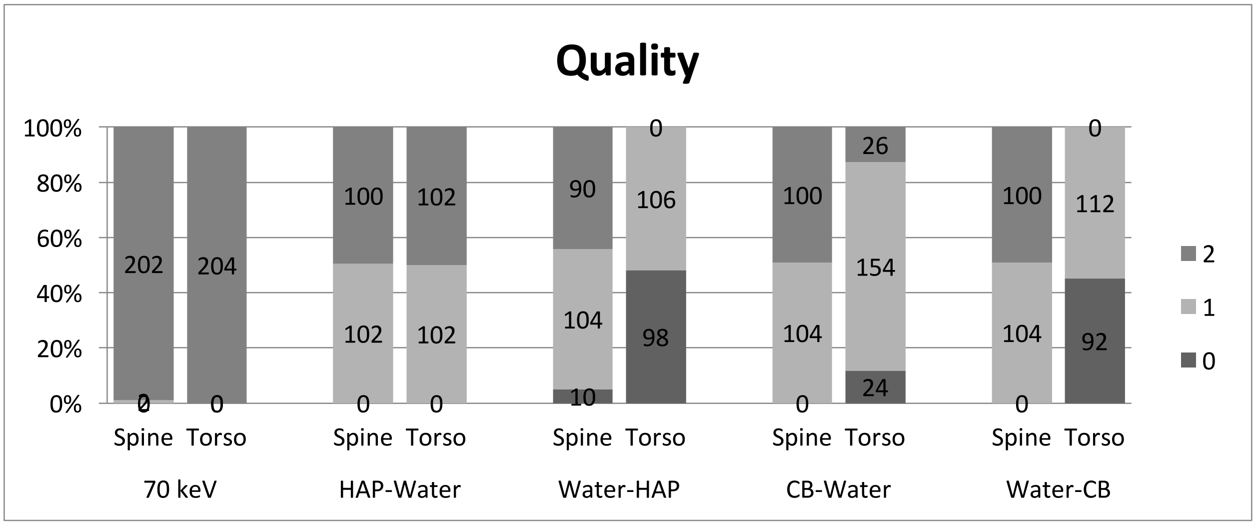

Figure 10: Image quality score in 5 different algorithms, sorted by phantom type. Score 0, artifact makes image non-diagnostic; Score 1, artifact present but still be able to make a diagnosis; Score 2, no significant artifact. (“Spine” stood for spine phantom without torso phantom encasement; “Torso” stood for spine phantom with torso phantom encasement.)

3.2 Patient studies results

There were 1251 patients with confirmed spine metastases from January 2014 to March 2017. Among them, 32 patients underwent DECT scans within 30 days either before or after the diagnosis. After measuring the ROIs of tumors and background bone marrow compartment, we exclude 26 patients whose tumors were too obvious on 70-keV reconstruction (difference >100HU from bone marrow compartment). Finally, we found 6 patients, 24 segments of lumbar spine (we excluded L1-L3 vertebrae in one patient due to post-operation artifacts; one patient's pelvic CT scan only include L4 and L5 vertebrae), with 9 eligible tumors to validate our algorithms. Two reviewers read the images in the same method as that in phantom study without other clinical information.

The combined results from two readers are summarized in Table 3.

CT image reconstruction	Tumor detection rate (%) (Tumor detected/18 eligible tumors)	False positive rate (%) (False positive/30 spine without tumors)
70 keV	55.56% (10/18)	0 (0/30)
HAP-Water	77.78% (14/18)	6.67% (2/30)
Water-HAP	22.22% (4/18)	26.67% (8/30)
CB-Water	61.11% (11/18)	6.67% (2/30)
Water-CB	38.89% (7/18)	13.3% (4/30)

Table 3: The tumor detection rate and the false positive rate in different algorithms.

4 DISCUSSION

4.1 Performance of material decomposition algorithms

In our study, the sensitivity of the 70 keV virtual monochromatic spectral images (resembling conventional 120 kVp polychromatic CT images) of the torso encasement phantom is 72% (95% CI, 66%-78%), close to the sensitivity of conventional CT from meta-analysis and literature review, which was 77.1%[6]. This finding could justify the usage of our torso encasement phantom with 70 keV reconstruction as reference when examining the diagnostic power of other algorithms. Based on this prerequisite, we found that for isodense lesions, DECT using the HAP-Water algorithms had a better sensitivity than the 70 keV reconstruction, while yielding an equivalent specificity, which meant that this algorithm had a better diagnostic performance. Furthermore, the high inter-reviewer reliability of HAP-Water algorithm also implied that DECT could help decrease the image ambiguity, make it more favorable for clinical use.

In clinical practice, abdomen CT scans of cancer patients were mainly used for evaluating primary tumors or monitoring treatment response in solid organs, rather than for detecting subtle spine metastases. Therefore, spine metastases would be easily missed on routine CT scans if not being conspicuous under the default CT window. Our study showed that the HAP-Water algorithm could provide better tumor conspicuity, thus enabling readers to detect these incidental but clinically important abnormalities without adjusting the window-level (Figure 11).

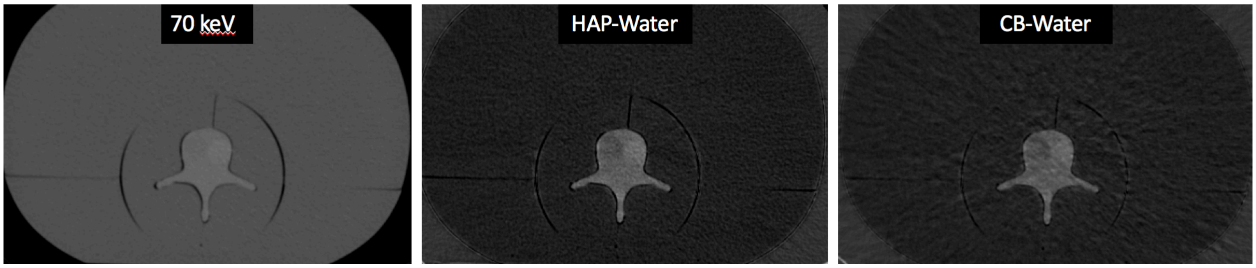

Figure 11. A torso phantom encasement with a mild sclerotic tumor embedded in the left side and a mild lytic tumor in the right side of the vertebral body.
Under default window, the tumor was hardly discernable in 70 keV image (Left). In HAP-Water (Middle) and CB-Water (Right) reconstruction, the lytic tumor became darker because of less calcium content and more discernable. The sclerotic tumor brightened up because of its higher calcium content.

For sclerotic and osteolytic lesions, the HAP-Water algorithm did not demonstrate a significantly better sensitivity than 70 keV reconstruction probably because of two reasons. First, 70 keV reconstruction already achieve good sensitivity and specificity in detecting sclerotic and osteolytic lesions so that the superiority of material decomposition became less significant.

Second, reviewers in this study were instructed to look for bone lesions, thus might scrutinize the images more carefully. As a result, subtle differences in HU between tumors and bone marrow compartment (-40HU in lytic lesions, +40 HU in sclerotic lesions) on 70 keV reconstruction became more easily detected.

4.2 Effect of torso phantom encasement

In this study, we found that the image quality of spine with torso phantom encasement was worse than the spine phantom without torso encasement. This result might be due to three reasons: beam-hardening effect, imperfect spectral filtration using single X-ray source, and scatter artifacts. Beam-hardening occur when x-rays pass through objects because the attenuation of the low energy photons is greater than high energy photons; therefore, the remaining x-ray beam contains more high energy photons and does not follow the simple exponential decay as it is in a monochromatic X-ray [22]. These artifacts are more prominent when x-rays pass through thick soft tissue (the torso phantoms encasement in our study), or through high effective atomic number material (such as metal). Although dual energy CT can theoretically help eliminate beam-hardening artifacts in reconstructed high keV virtual monochromatic images, such a conclusion is based on the assumption of x-ray absorption spectrum not affected by K-edge. In reality, the x-ray absorption spectrums are rarely in their ideal shape[23]. Therefore, the more severe beam-hardening artifacts associated with torso phantoms encasement may not be completely eliminated by DECT, thus leading to worse image quality.

The DECT used in this study has only one x-ray source, and perfect spectral filtration for both the low- and high-energy images is difficult with rapid-switching single source CT[24]. Lastly, artifact caused by scatter are proportional to the density of material traversed and not corrected by DECT, contributing to the poorer image quality in the torso phantom encasement (Figure 12).

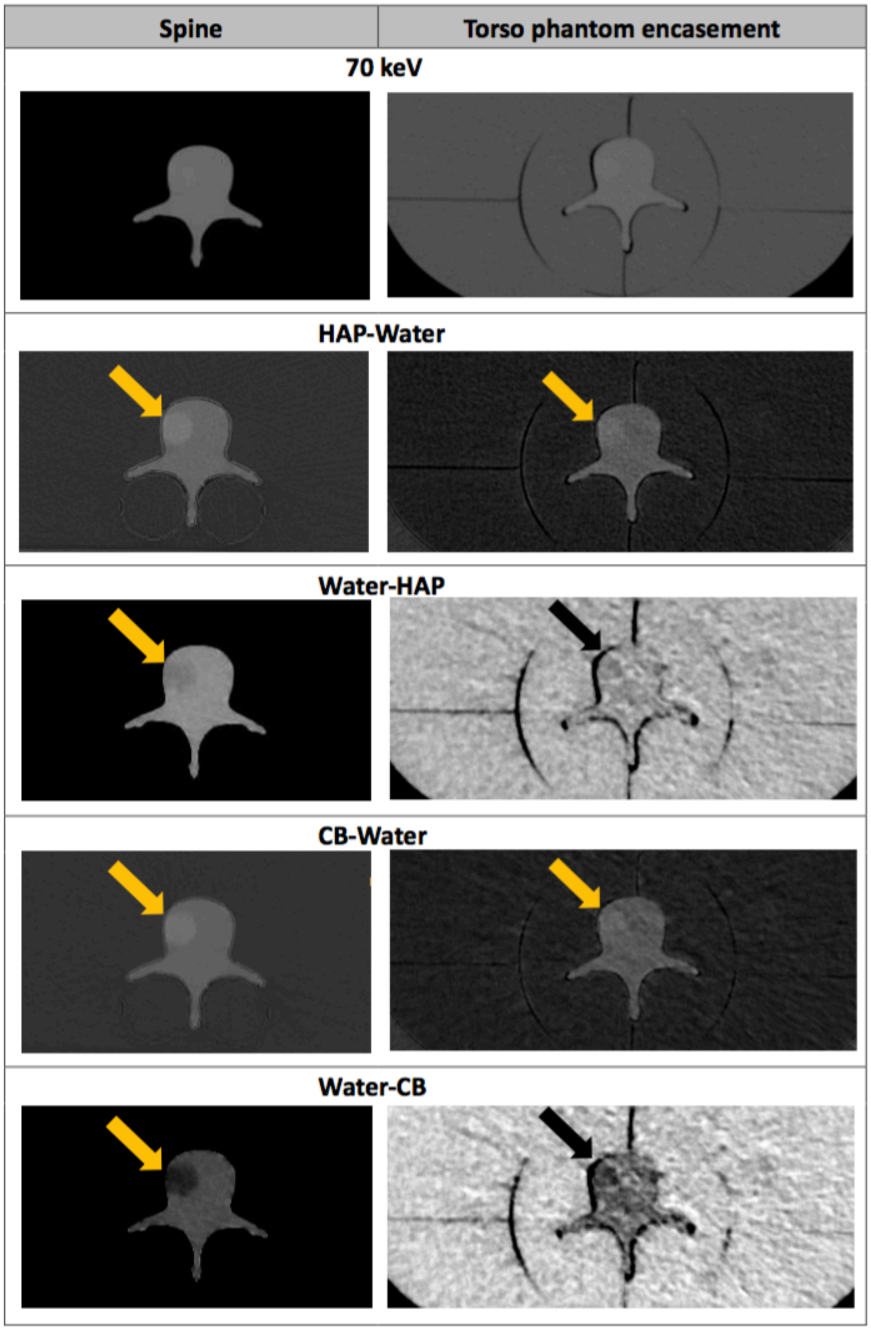

Figure 12. The same spine scan without (left) and with torso phantom encasement (right). The image quality was similar between without and with torso phantom encasement in 70 keV and HAP-Water images. In contrast, the image quality was worse with torso phantom encasement in Water-HAP, CB-Water, and Water-CB algorithms.

4.3 Effect of reconstruction algorithms

In our study, the image quality of 70 keV virtual monochromatic reconstructed images was better than 4 other material decomposition algorithms been tested, regardless of phantom type. This phenomenon also occurred in Winklhofer et al's study[25] of images from phantoms and patients, showing that the rapid-kilovoltage-switching DECT material decomposition images suffered from more severe beam-hardening artifacts than the virtual monochromatic images. Since the concept of two material decomposition algorithm of DECT is that any material's attenuation coefficient can be considered as a linear combination of the attenuation coefficients of two other constituent materials[24], the original artifacts will also be erroneously expressed in the material decomposition images, compromising their image quality.

Among the four material decomposition algorithms of DECT, image quality was best in the HAP-Water algorithm, followed by CB-Water algorithm, and worst in the Water-HAP and Water-CB algorithms. Based on the NIST database of attenuation coefficient, the hydroxyapatite has higher dual energy ratio (i.e., the CT number measured in the low-energy divided by that measured in the high-energy image) than the cortical bone. Water, by definition, the CT number is always 0 regardless of energy change (Figure 7). Scatter artifacts would prone to be misclassified as water and expressed in water images because it is almost independent of photon energy[25]. This misclassification will decrease the diagnostic performance of Water-HAP and Water-CB algorithms. In contrast, the high dual energy ratio of the hydroxyapatite makes it less susceptible to artifacts misclassification.

4.4 Patient studies

The main purpose of our patient study was to validate the algorithms we developed from phantom studies. To demonstrate the superiority of DECT in showing isodense bone lesions that were usually subtle in conventional CT, we only selected tumors with a HU difference less than 100HU. At our institution, routine CT is performed with DECT only if the CT scanner is capable of DECT and when the radiation dose can be set to approximate that of conventional single-energy CT; as a result, about one-third of examinations would preclude the use of DECT[25]. Because of the limited percentage of patients receiving their examinations with DECT, as well as the strict inclusion criteria for hardly discernable tumors, we only found 6 patients with 9 eligible lesions, which were not enough for statistical analysis. Nevertheless, even with these few cases, we still found that the material decomposition algorithms could help pick up tumors initially missed on the conventional CT (Figure 13, 14).

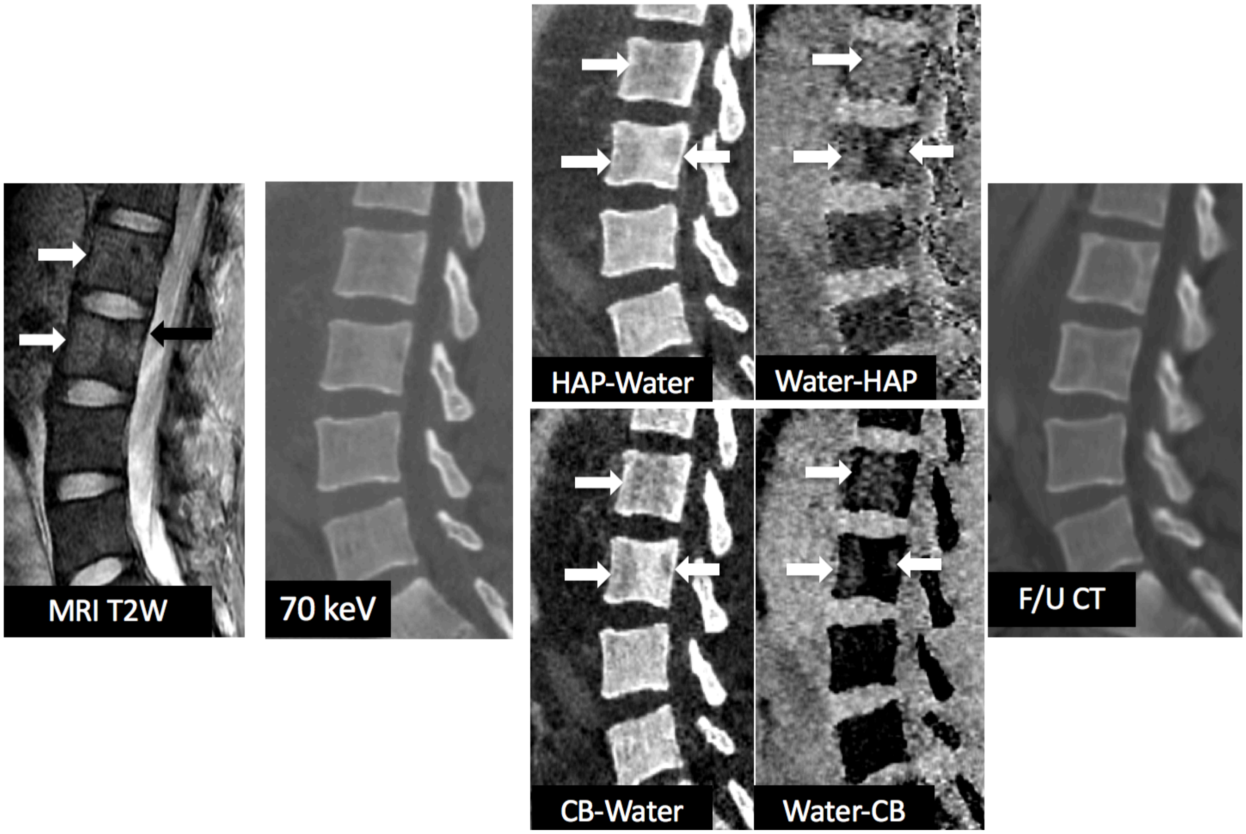

Figure 13. A 28-year-old male with testicular cancer.
Initially, there were suspicious spine metastases on T2W MRI. The DECT done within 8 days from the MRI scans was read as negative on 70 keV reconstruction. After material decomposition algorithms, the tumors were clearly seen in HAP-Water and CB-Water with corresponding changes in the Water-HAP and Water-CB images. Both readers picked up these lesions.
The follow up single energy CT done 4 months later showed there were osteolytic lesions with sclerotic margin at the same anatomical location that the material decomposition images demonstrated before.

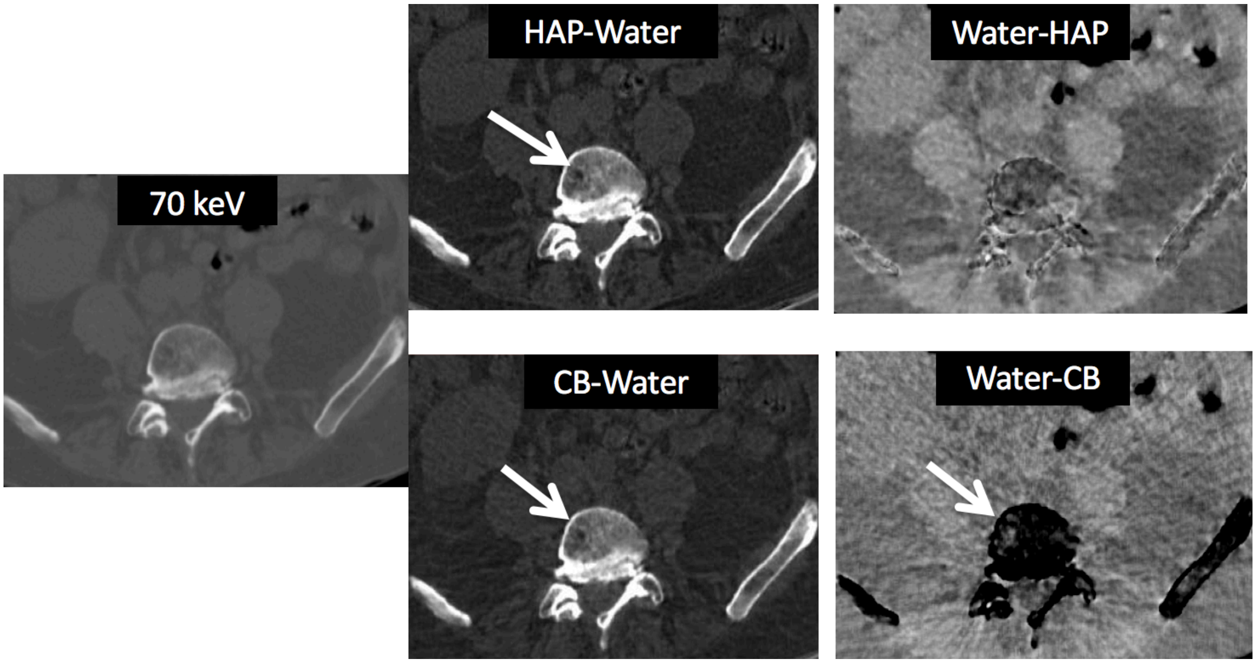

Figure 14. A 74-year-old male with multiple myeloma. The DECT with 70 keV reconstruction showed subtle mixed osteolytic and osteosclerotic lesions in the right aspect of vertebral body. After material decomposition algorithms, the tumors became more discernable in HAP-Water and CB-Water with corresponding changes in the Water-CB images (arrows). No tumor was detected in Water-HAP image due to severe artifacts.

After these patient images were re-analyzed by our readers, the tumor detection rate was higher in the HAP-Water images, not jeopardized by artifacts. These findings were compatible with the results from our phantom studies that HAP-Water algorithm had a higher sensitivity and was less affected by artifacts. Similarly, the higher false positive rate and lower tumor detection rate in the Water-HAP and Water-CB images, compared to 70 keV reconstruction, were also correlated to our findings that both water images were more prone to artifacts and thereby less sensitive. (Figure 15).

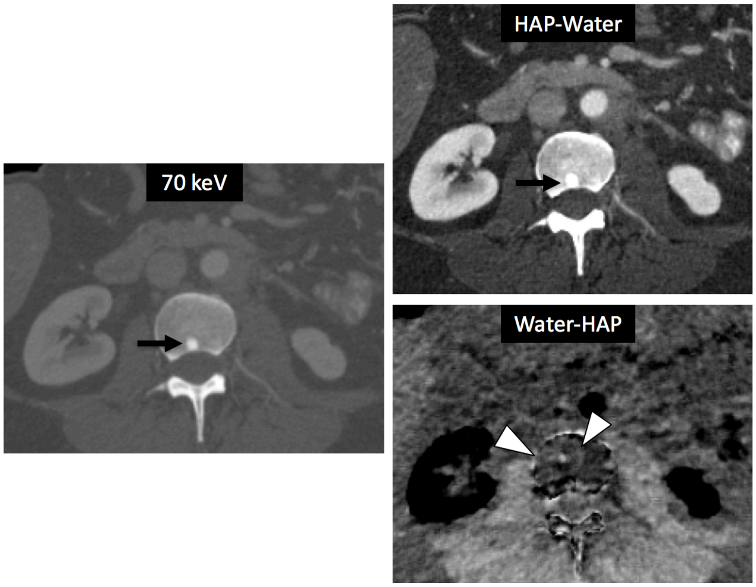

Figure 15.
A 47-year-old female with breast cancer.
Besides the punctate sclerotic spine metastasis(arrow), one reader falsely diagnosed a space occupying tumor in the right side of vertebral body in Water-HAP image (arrow head).

4.5 Clinical application

Cancer patients usually undergo whole-body imaging studies only once for cancer staging before starting treatment. After that, to reduce unnecessary radiation exposure, follow-up CT scans are often region specific. Our study results suggested that the usage of DECT and material decomposition algorithm might enable the detection of subtle spine metastases, which are known to be easily missed by conventional CT scans. In addition, studies have shown that overt sclerotic bone metastases usually cause less pain and less disability to cancer patients, while mixed type and lytic type metastases can have greater impact on the quality of life and should to be treated more aggressively[26]; hence the greater ability of exhibiting isodense bone tumors can help guiding the treatment, reducing the suffering of cancer patients. Most importantly, this diagnostic competence is based upon the nature of tissue type, regardless of the presence of iodinated contrast, and can be widely applied to every patient with suspected bone metastases.

4.6 Limitation

There are several limitations in this study. First, we did not perform quantitative and qualitative analysis on patient images because of the small number of cases identified during retrospective medical record review. We only included patients whose confirmed lumbar spine metastases were not obvious (less than 100HU difference in tumor and marrow compartment) on the 70 keV reconstruction, therefore limiting the number of eligible case. Second, we only tested our phantoms in one type of DECT machine (single source rapid-kilovoltage-switching). The results might vary using different types of scanners such as dual source DECT or CT with photon counting detectors. Third, this study could potentially possess reviewer bias because reviewers might be inclined to look for bone lesions and increase the sensitivity in detecting true lesions. Finally, different reconstruction algorithms (e.g., the usage of three-material decomposition algorithm) could also result in different material separation capability and accuracy, which need to be further explored in the future.

5 CONCLUSION

DECT with hydroxyapatite-water material decomposition may help detect spine marrow metastases, especially for subtle isodense tumors. Further study in prospective clinical scans is warranted.

6 REFERENCES

1. The Organisation for Economic Co-operation and Development (OECD). Health Care Utilisation. https://stats.oecd.org/Index.aspx?DataSetCode=HEALTH_PROC.
2. Coburn N, Przybysz R, Barbera L, Hodgson DC, Laupacis A, Law C. Evaluation of CT and MRI scanning among cancer patients. *J Clin Imaging*. 2011;35(4):301-308.
3. Guillevin R, Vallee JN, Lafitte F, Menuel C, Duverneuil NM, Chiras J. Spine metastasis imaging: review of the literature. *J Neuroradiol*. 2007;34(5):311-321.
4. Mundy GR. Metastasis to bone: causes, consequences and therapeutic opportunities. *Nat Rev Cancer*. 2002;2(8):584-593.
5. Rybak LD, Rosenthal DI. Radiological imaging for the diagnosis of bone metastases. *Q J Nucl Med*. 2001;45(1):53-64.
6. Yang HL, Liu T, Wang XM, Xu Y, Deng SM. Diagnosis of bone metastases: A meta-analysis comparing 18FDG PET, CT, MRI and bone scintigraphy. *Eur Radiol*. 2011;21(12):2604-2617.
7. Qu X, Huang X, Yan W, Wu L, Dai K. A meta-analysis of ^{18}FDG-PET-CT, ^{18}FDG-PET, MRI and bone scintigraphy for diagnosis of bone metastases in patients with lung cancer. *Eur J Radiol*. 2012;81(5):1007-1015.
8. Liu T, Wang S, Liu H, et al. Detection of vertebral metastases : a meta - analysis comparing. *J Cancer Res Clin Oncol*. 2017;143(3):457-465.
9. Coursey C a, Nelson RC, Boll DT, et al. Dual-energy multidetector CT: how does it work, what can it tell us, and when can we use it in abdominopelvic imaging? *Radiographics*. 2010;30(4):1037-1055
10. Siegel MJ, Kaza RK, Bolus DN, et al. White Paper of the Society of Computed Body Tomography and Magnetic Resonance on Dual-Energy CT , Part 1 : Technology and Terminology. *J Comput Assist Tomogr*. 2016;40(6):841-845.
11. Kaup M, Wichmann JL, Beeres M, et al. Dual-Energy CT – based Display of Bone Marrow Edema in Osteoporotic Vertebral Compression Fractures : Impact on Diagnostic Accuracy of Radiologists with Varying Levels of Experience in Correlation to MR Imaging. *Radiology*. 2016;280(2).
12. Pache G, Krauss B, Strohm P, et al. Dual-Energy CT Virtual Noncalcium Technique: Detecting Posttraumatic Bone Marrow Lesions—Feasibility Study. *Radiology*.

2010;256(2):617-624.

13. Mallinson PI, Coupal TM, Mclaughlin PD, Munk PL, Ouellette HA. Dual-Energy CT for the Musculoskeletal System. *Radiology*. 2016;281(3).
14. Lee YH, Kim S, Lim D, Suh J-S, Song H-T. Spectral parametric segmentation of contrast-enhanced dual-energy CT to detect bone metastasis: feasibility sensitivity study using whole-body bone scintigraphy. *Acta Radiol*. 2014;0(0):1-7.
15. Witham TF, Khavkin YA, Gallia GL, Wolinsky J-P, Gokaslan ZL. Surgery Insight: current management of epidural spinal cord compression from metastatic spine disease. *Nat Clin Pr Neuro*. 2006;2(2):87-94.
16. Kugel H, Jung C, Schulte O, Heindel W. Age- and sex-specific differences in the 1H-spectrum of vertebral bone marrow. *J Magn Reson Imaging*. 2001;13(2):263-268.
17. Fitzgerald PF, Colborn RE, Edic PM, et al. CT Image Contrast of High-Z Elements: Phantom Imaging Studies and Clinical Implications. *Radiology*. 2016;0(0):1-11.
18. Arthur C. Guyton JEH. *Textbook of Medical Physiology*. 10th ed. Philadelphia: Saunders; 2005.
19. Matsumoto K, Jinzaki M, Tanami Y, Ueno A, Yamada M, Kuribayashi S. Virtual Monochromatic Spectral Imaging with Fast Kilovoltage Switching: Improved Image Quality as Compared with That Obtained with Conventional 120-kVp CT. *Radiology*. 2011;259(1):257-262.
20. X-Ray Mass Attenuation Coefficients-National Institute of Standards and Technology (NIST). https://physics.nist.gov/PhysRefData/XrayMassCoef/tab2.html.
21. Viera AJ, Garrett JM. Kappa_statisitc_paper. *Fam Med*. 2005;37(5):360-363.
22. Boas FE, Fleischmann D. CT artifacts: causes and reduction techniques. *Imaging Med*. 2012;4(2):229-240.
23. Alvarez R, Macovski A. Energy-selective recon- structions in x-ray computerized tomography. *Phys Med Biol*. 1976;21:733–744.
24. McCollough CH, Leng S, Yu L, Fletcher JG. Dual- and Multi-Energy CT: Principles, Technical Approaches, and Clinical Applications. *Radiology*. 2015;276(3):637-653.
25. Winklhofer S, Lambert JW, Sun Y, Wang ZJ, Sun DS, Yeh BM. Pelvic Beam-Hardening Artifacts in Dual-Energy CT Image Reconstructions: Occurrence and Impact on Image Quality. *Am J Roentgenol*. 2016;208(1):114-123.
26. Vassiliou V, Kalogeropoulou C, Petsas T, et al. Clinical and radiological evaluation of

patients with lytic, mixed and sclerotic bone metastases from solid tumors: is there a correlation between clinical status of patients and type of bone metastases? *Clin Exp Metastasis*. 2007;24(1):97-103.

Publishing Agreement

It is the policy of the University to encourage the distribution of all theses, dissertations, and manuscripts. Copies of all UCSF theses, dissertations, and manuscripts will be routed to the library via the Graduate Division. The library will make all theses, dissertations, and manuscripts accessible to the public and will preserve these to the best of their abilities, in perpetuity.

Please sign the following statement:

I hereby grant permission to the Graduate Division of the University of California, San Francisco to release copies of my thesis, dissertation, or manuscript to the Campus Library to provide access and preservation, in whole or in part, in perpetuity.

Hsu-Cheng Huang
Author Signature

8-25-2017
Date